The Effect of Thermal Creep Flow in a Heat Assisted Magnetic Recording System

By

Joanna Bechtel

BS (University of Illinois Urbana-Champaign) 2007

A report submitted in partial satisfaction of the
Requirements for the degree of

Masters of Science, Plan II

in

Mechanical Engineering

at the

University of California at Berkeley

Committee in Charge:

Professor David B. Bogy, Chairman

Professor Costas P. Grigoropoulos

Fall Semester 2009

Abstract

New nanoscale heat transfer effects are introduced in a heat assisted magnetic recording hard disk drives, a potential new technology to increase recording density. One such effect is thermal creep, a rarefied gas phenomena in which a tangential boundary temperature gradient drives fluid flow from cold to hot. Thermal creep has been added to an air bearing finite volume solver. Poiseuille and thermal creep non-dimensionalized flow rate coefficient databases were generated using Chebyshev polynomial expansions and the variational method. The simple case of an infinite parallel plate-slider configuration was simulated and compared very well with semi-analyical results. Some preliminary trailing pad simulation results are presented. The contribution of thermal creep arising from laser heating of the disk is to slightly enhance the air bearing mass flow rate locally around the laser spot. The length scale of the laser spot was too small to effect the pressure distribution significantly or alter the pressure force. Future work will determine if the temperature gradient on the slider surface has a notable effect on pressure vis thermal creep.

Contents

List of Figures

List of Tables

Nomenclature

$\overline{c}$	average molecular speed
$C_n(x)$	Chebyshev polynomial of the first kind, $\cos(n\cos^{-1}(x))$
D	inverse Knudsen number, $\sqrt{\pi}/2\text{Kn}$
h	channel height or lubricating film thickness [m]
h_m	minimum (characteristic) spacing [m]
H	nondimensional spacing, h/h_m
Kn	Knudsen number, λ/h
L	slider (characteristic) length [m]
k	modified Knudsen number, $(2/\sqrt{\pi})\text{Kn} = 1/D$
$\dot{M}$,	mass flowrate per unit channel width, [kg/s/m]
P	nondimensional local pressure, p/p_0
p	local pressure [Pa]
p_0	ambient pressure [Pa], usually 1 atm
Q_P, Q_T	non-dimensionalized flow rate coefficient
Q_{con}	flow rate coefficient for Poiseuille flow, $D/6$
$\overline{Q}_P$, $\overline{Q}_T$	relative non-dimensionalized flow rate coefficient, Q/Q_{con}
T	temperature, [K or °C]
T_0	characteristic temperature, [K or °C], usually 25°C
$T_n(Z)$	Abramowitz function, $\int_0^\infty t^n \cdot \exp\left(-t^2 - \frac{Z}{t}\right) dt$
U	boundary speed [m/s]
u, v, w	x, y, z components of velocity
x, y, z	Cartesian coordinates with x being the flow and slider length direction, y the width direction into the page, and z the film thickness direction
X, Y, Z	nondimensional coordinates, $x/L, y/L, z/h_m$
Γ	diffusion coefficient, $\overline{Q}_P P H^3$ for the FK lubrication equation
λ	molecular mean free path [m]
Λ	bearing number, $u\frac{6\mu L}{p_a h_m^2}$
μ	viscosity [kg/s/m=Pa·s]
ϕ	perturbed quantity of flow velocity distribution, $f/f_0 - 1$
ρ	density [kg/m^3]
σ_v	momentum accommodation coefficient
τ	nondimensional temperature, $T/T_0 - 1$

Subscripts

P	Poiseuille flow
C	Couette flow
T	thermal creep flow
w	boundary

Introduction

The Information Storage Industry Constortium has announced the goals of demonstrating stable hard disk magnetic recording technology at areal densities of 4 Tb/in^2 by early 2013 and up to 10 Tb/in^2 by the end of 2015 [6]. The super-paramagnetic limit poses a barrier when scaling down traditional hard disk drive technologies– beyond this threshold signal-to-noise, thermal stability, and writability are compromised. A new technology known as heat-assisted magnetic recording (HAMR) uses a higher coercivity magnetic media that is thermally stable at room temperature with very small grain sizes, but also introduces new tribological, material, and heat transfer challenges.

HAMR requires the local heating of the magnetic media to several hundreds of degrees within a nanosecond. With such high temperatures required for recording, the disk lubricant can start to desorb and/or degrade which can lead to catastrophic head-disk interface failure. Moreover, the effects associated with the rapid temperature rises and high temperature gradients at nanoscales also could further exacerbate the head-media interface stability. Due to the scale and complexity of the HAMR system, direct experimental diagnosis is very challenging. On the other hand, numerical modeling and simulation can provide more quantitative results and insightful information, and is preferable due to its convenience and cost-effectiveness. Yet, the HAMR system also provides many modeling challenges in numerical simulations.

The HAMR system is outside the range of classical theory due to rarefaction and compressibility effects in the air bearing and the nanoscale dimensions. Rough estimates indicate that a laser spot on the order of $(12\text{ nm})^2$ and a slider-disk spacing of 2.5 nm is needed to achieve 4 Tb/in^2. The laser system integrated into the slider will dissipate energy into the slider and cause thermal distortion, affecting flying height and pitch [2, 18]. The lubricant and magnetic media undergo flash heating as the temperature reaches 350°C or more above ambient temperature within 1 ns and rapidly cool back to ambient [3]. A robust lubricant must be designed to withstand rapid temperature rises and large thermal gradients in order to avoid lubricant depletion by evaporation or thermocapillary stress [17]. Thus there are many new nanoscale thermal effects to consider and investigate.

This report details the first step in developing a HAMR model: adding thermal creep flow to the air bearing governing equation and studying its effects on the air bearing flow. In a rarefied gas, it is possible to start and maintain gas flow with a tangential temperature gradient in the boundary wall. In a traditional hard disk drive (HDD), even thermally actuated sliders, the temperature gradients in the slider and disk are zero or negligible and thermal creep flow is not present. However, very large temperature gradients will exist in the disk around the laser spot. Even though the laser spot is very small (< 100 nm), the resulting temperature gradient is so large (increase of 350°C in 7 nm) that thermal creep will enhance the airflow locally. The first chapter describes the fundamentals of the thermal creep phenomena. The second chapter describes how to create databases for the Poiseuille and thermal creep flow rate coefficients that appear in the governing generalized lubrication-type equation. In the third chapter the finite volume discretization including thermal creep is described. Semi-analytical solutions to the simple problem of an infinitely long parallel plate-slider are shown in the fourth chapter. The fifth chapter presents the results of a numerical simulation of this same problem using the static solver CMLAir QuickHAMR that includes thermal creep. Preliminary trailing pad simulation results are presented in chapter six. The concluding seventh chapter describes future work to continue to add to the HAMR numerical simulation.

Chapter 1

Thermal Creep Fundamentals

A tangential temperature gradient along a channel wall can drive flow in a rarefied gas from *from cold to hot*. This phenomenon is called thermal creep or thermal transpiration. The following explanation of thermal creep fundamentals is based on Section 5.1 in [11].

Consider two tanks both filled with the same and kept at the same pressure initially ($p_1 = p_2$) but different temperatures ($T_1 > T_2$) and connected by a channel as shown in Figure 1.1. In the familiar continuum regime where the channel is relatively thick ($\lambda \ll h$, Kn < 0.01), the equilibrium condition is no flow in the channel. However, if the channel thickness h is comparable in magnitude to the mean free path λ, the interaction of the gas molecules with the channel walls is significant and rarefied gas effects must be considered. For simplification, consider the free molecular regime ($\lambda \gg h$, Kn > 10) where intermolecular collisions are negligible compared to molecule-wall interactions. Furthermore, consider specular reflection of the molecules from the boundary: the tangential velocity of the reflected molecules is unchanged but the normal velocity is reversed ($\sigma_v = 0$).

Assume that the fluid density ρ is proportional to the number of molecules per unit volume n and temperature of the fluid T is proportional to the square of the average molecular speed $\bar{c}^2$. Take m to be the mass of a gas molecule and the equation of state to be $p = \rho RT$. The mass fluxes at the hot and cold ends are $mn_1\bar{c}_1$ and $mn_2\bar{c}_2$ respectively.

$$\frac{mn_1\bar{c}_1}{mn_2\bar{c}_2} \approx \frac{\rho_1}{\rho_2}\sqrt{\frac{T_1}{T_2}} = \frac{p_1}{p_2}\sqrt{\frac{T_2}{T_1}} = \sqrt{\frac{T_2}{T_1}} \leq 1$$

So the mass flux at the hot end is less than the mass flux at the cold. This exercise indicates that fluid is creeping form cold to hot.

In rarefied gas flows where channels in atmospheric conditions have characteristic dimensions of the same order or smaller than the mean free path of the

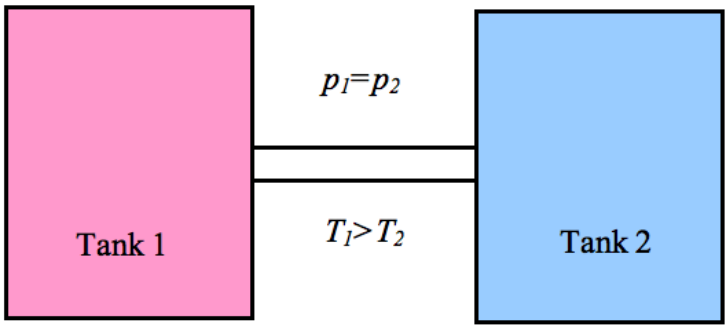

Figure 1.1: Thermal creep illustrative problem: two tanks at the same pressure and different temperature connected by a microchannel.

molecules or channels where the pressure is low, thermal creep effects can be significant. The purpose of this report is to determine if very large but localized boundary temperature gradients on the disk surface will mean thermal creep flow is significant in a HAMR HDD.

Chapter 2

Flow Rate Coefficient Databases

The Reynolds-type lubrication equation derived by Fukui and Kaneko [8] from the linearized Boltzmann equation governs the air bearing problem. The one dimensional steady-state form is:

$$\frac{d}{dX}\left\{\overline{Q}_P(D)\frac{dP}{dX}PH^3 - \overline{Q}_T(D)\frac{d\tau_w}{dX}P^2H^3 - \Lambda PH\right\} = 0 \tag{2.1}$$

Students in the Computer Mechanics Laboratory have developed a static air bearing solver, CMLAir Quick 4.32, to solve this equation (without thermal creep, i.e. $\frac{d\tau_w}{dX} = 0$) for the unknown P in traditional HDDs. Equation 2.1 is discretized using a finite volume formulation and then solved iteratively with a multigrid solver. The relative non-dimensionalized Poiseuille flow rate coefficient Q_P, which depends on local pressure P and spacing H, is quickly obtained at each location on the slider by look-up in a database created at the beginning of the simulation. In order to add thermal creep to the finite volume formulation, a similar database needs to be created for Q_T. As this chapter will explain, the Quick 4.32 method of determining Q_P is not adequate for Q_T, so a new technique had to be developed.

2.1 Poiseuille Flow Rate Coefficient

In Equation 2.1 the flow rate coefficients are cast as relative flow rates: the ratio of $Q_P(D)$ and $Q_T(D)$ to $Q_{con} = D/6$, the flow rate coefficient for continuum Poiseuille flows. They are functions of the inverse Knudsen number D which can be written in terms of a characteristic inverse Knudsen number D_0, non-dimensional pressure P and spacing H:

$$D = D_0PH \tag{2.2}$$

The integro-differnetial equations for Poiseuille flow velocity profiles for diffuse reflection of gas molecules at boundary surfaces ($\sigma_v = 1$, molecules are reflected from

the walls with zero average tangential velocity) are given in [8] and summarized here. The perturbed quantity of Poiseuille flow velocity is determined from the linearized Boltzmann equation and found to be:

$$\phi_P(Z) = 1 + \frac{1}{\sqrt{\pi}k_0}\int_0^H T_{-1}\left(\frac{|Z-Z'|}{k_0}\right)\cdot\phi_P(Z')dZ' \tag{2.3}$$

where T_n is the Abramowitz function

$$T_n(Z) = \int_0^\infty t^n\cdot\exp\left(-t^2-\frac{Z}{t}\right)dt \tag{2.4}$$

The non-dimensional flow rate is given by the expression

$$Q_P(D) = -\frac{1}{D} + \frac{1}{D^2}\int_0^H \phi_P(Z)dZ \tag{2.5}$$

Equation 2.3 can be transformed into a system of linear algebraic equations by casting it in a finite difference formulation. As shown in [9], discretize the spacing H by n grid points with a spacing $\Delta = H/n$ and solve for the unknown Poiseuille velocity perturbation $(\phi_P)_j$ at each grid point $Z_j = \Delta\cdot(j-\frac{1}{2})$. The system of equations for the vector of Poiseuille velocity perturbations at each grid point ϕ_P is:

$$\sum_{j=1}^{n} A_{ij}(\phi_P)_j = 1 \tag{2.6}$$

where

$$A_{ij} = \begin{cases} \delta_{ij} - \frac{1}{\sqrt{\pi}}\left[T_0\left(\left|\frac{Z_i-Z_j}{k_0}\right| - \frac{\Delta}{2k_0}\right) - T_0\left(\left|\frac{Z_i-Z_j}{k_0}\right| + \frac{\Delta}{2k_0}\right)\right] & \text{if } i\neq j \\ \frac{2}{\sqrt{\pi}}T_0\left(\frac{\Delta}{2k_0}\right) & \text{if } i = j \end{cases} \tag{2.7}$$

where T_0 is the Abramowitz function for $n = 0$ given in Equation 2.4 and $k_0 = \frac{1}{D_0}$ is characteristic modified Knudsen number. Then the Poiseuille flow rate coefficient is

$$Q_P = -\frac{1}{D} + \frac{1}{D^2}\Delta\sum_{j=1}^{n}(\phi_P)_j \tag{2.8}$$

For a range of inverse Knudsen numbers $0.001 < D < 100$, published results of this numerical method [9, 13] are plotted with the independent results of this author in Figure 2.1. Agreement is very good, and the curves practically lie on top of each other.

However, the numerical method is fairly computationally expensive. Loyalka has demonstrated that variational results are within 1% of the more accurate

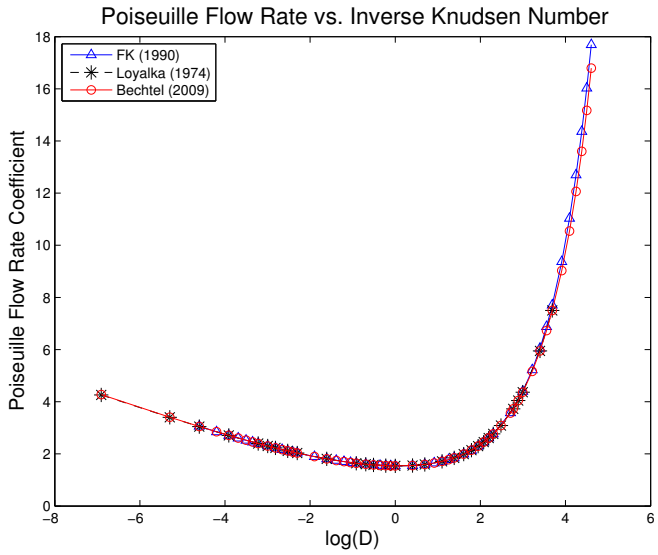

Figure 2.1: Q_P results with the finite difference numerical method described by Equations 2.6-2.8 published in [9, 13] and reproduced by the author

finite difference results [13]. Thus CMLAir developers chose to use the variational results to generate an extensive Q_P database for various D at the beginning of each simulation, a much larger database than the that published in [9]. The variational result of Loyalka for Poiseuille flow:

$$Q_P(D) = -\frac{1}{D} + \frac{1}{\Delta}\left(C_{11} - \frac{D^2}{6}C_{12} + \frac{D^4}{144}C_{22}\right) \tag{2.9}$$

where the constants C_{11}, C_{22} and C_{12} depend on $T_0(Z), T_1(Z)$, and $T_2(Z)$ and are given in Appendix 2 of [8]. Thus a method must be developed to evaluate the the Abramowitz function for $n = 1, 2, 3$. Currently in CMLAir Quick 4.32, $T_n(Z)$ is evaluated by its power series representation for $D < 1.1$ and the asymptotic expansion for $D \geq 1.1$. The power series representations and asymptotic expansions are given in [1, p. 1001]. This piecewise method of evaluating $T_n(Z)$ results in a database of Q_P computed very quickly that closely matches the finite difference method results.

2.2 Thermal Creep Flow Rate Coefficient

Similar to ϕ_P, the thermal creep velocity perturbation ϕ_T is governed by an integro-differential equation [8]:

$$\phi_T(Z) = \frac{1}{2} + \frac{1}{\sqrt{\pi}k_0}\int_0^H T_{-1}\left(\frac{|Z-Z'|}{k_0}\right)\cdot\phi_T dZ' + \frac{1}{\sqrt{\pi}k_0}\int_0^H T_1\left(\frac{|Z-Z'|}{k_0}\right)dZ' \tag{2.10}$$

The non-dimensional flow rate is given by the expression

$$Q_T(D) = -\frac{2}{D^2}\int_0^H \phi_T(Z)dZ + Q_P \tag{2.11}$$

A finite difference formulation gives a system of linear algebraic equations for ϕ_T [13]:

$$\sum_{j=1}^{n} A_{ij}(\phi_T)_j = S_i \tag{2.12}$$

where A_{ij} is the same as for ϕ_P in Equation 2.7 and S_i is defined as

$$S_i = S(Z_i) = \frac{1}{2} - \frac{1}{4\sqrt{\pi}}\left[T_0\left(\frac{H}{2}+Z\right) + T_0\left(\frac{H}{2}-Z\right)\right] - \frac{1}{2\sqrt{\pi}}\left[T_2\left(\frac{H}{2}+Z\right) + T_2\left(\frac{H}{2}-Z\right)\right] \tag{2.13}$$

The finite difference approximation of Q_T is

$$Q_T = -\frac{2}{D^2}\Delta\sum_{j=1}^{n}(\phi_T)_j + Q_P \tag{2.14}$$

For a range of inverse Knudsen numbers $0.001 < D < 100$, published results of this numerical method [13] are plotted with the independent results of this author in Figure 2.2. Agreement is very good, and the curves practically lie on top of each other as with Q_P.

To speed up computation time, use the variational result of Loyalka for thermal creep flow:

$$Q_T(D) = Q_T(D) = \frac{2}{D^2}\left(\frac{D^3}{12}\alpha_3 + D\alpha_4\right) - Q_P(D) \tag{2.15}$$

The coefficients α_3 and α_4 depend on $T_1(Z), T_2(Z), T_3(Z), T_4(Z)$, and $T_5(Z)$ and are given in Appendix 3 of [8]. Note that there is a typographical error in Equation 65 for the intermediate coefficient C_1': the first plus sign should be a minus sign.

Unfortunately, evaluating $T_n(Z)$ in a piecewise manner as was done for Q_P in CMLAir Quick 4.32 results in inaccurate results in the range $1.1 < D < 10$ as shown in Figure 2.3. The error in the asymptotic expansion of the Abramowitz

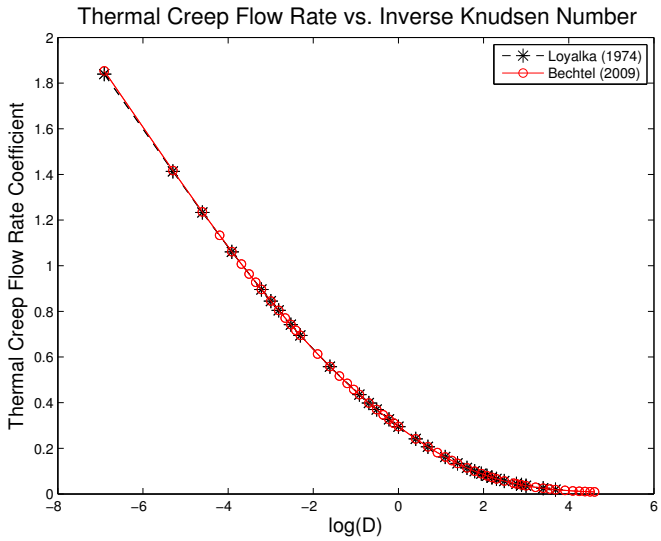

Figure 2.2: Q_T results of the finite difference numerical method described by Equations 2.12-2.14 published in [13] and reproduced by the author

function at those fairly small values compounds in the calculations (notice Q_P appears in Equation 2.11) and results in a hump in the blue curve of Figure 2.3. Thus a new method for evaluating T_n must be found.

As described by Macleod [15], Abramowitz functions can be expanded using Chebyshev polynomials of the first kind:

$$C_n(x) = \cos(n \cos^{-1}(x)); \tag{2.16}$$

Details of the expansion are simple but involved. A break-point value $a = 2$ was use, which Macleod determined to be optimal. The main advantage of this Chebyshev polynomial expansion is that the resulting Q_P and Q_T databases are accurate for the whole domain and no piecewise definitions are necessary. The Q_T results using Chebyshev polynomial expansions for T_n were practically the same as the numerical results in Figure 2.2. Thus this Chebyshev polynomial expansion was implemented in the under-development CMLAir QuickHAMR for both Q_P and Q_T. The Q_T database is the yellow curve plotted in Figure 2.3. The Q_P Chebyshev database matches the curves in Figure 2.1 for all practical purposes and a plot is not deemed necessary.

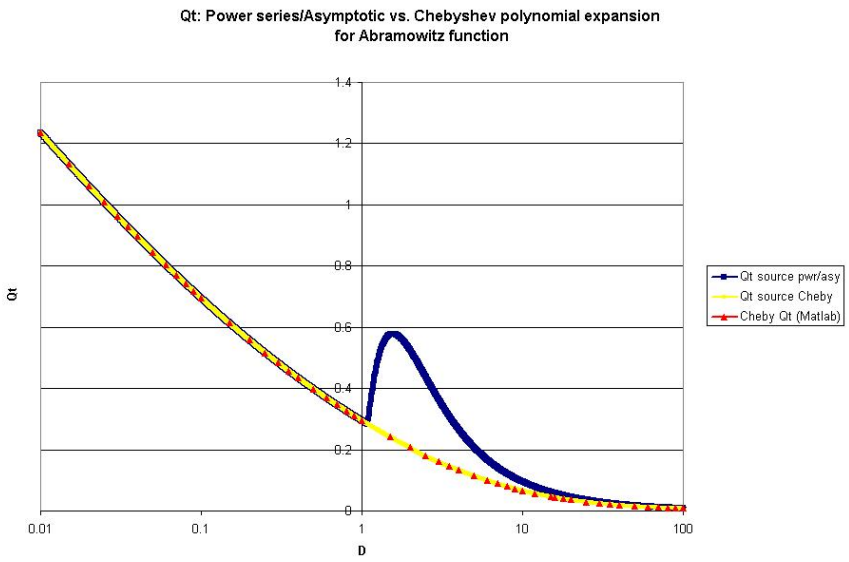

Figure 2.3: Q_T database results for the Abramowitz function evaluated with piecewise power series and asymptotic representation (blue curve) and Chebyshev polynomial expansions (yellow). The red triangles are the results from a MATLAB code using Chebyshev polynomials that matched finite difference numerical results almost exactly.

Chapter 3

Finite Volume Discretization

3.1 Differential Equations

In his book on numerical heat transfer fluid flow [16], Pantankar notes that relevant differential equations in physics indicate that the dependent variables of interest obey a general conservation principle:

$$\underbrace{\rho\frac{\partial\phi}{\partial t}}_{\text{unsteady}} + \underbrace{\text{div}\,(\rho\mathbf{u}\phi)}_{\text{convection}} = \underbrace{\text{div}(\Gamma\text{grad}\phi)}_{\text{diffusion}} + \underbrace{S}_{\text{source}} \tag{3.1}$$

In this general differential equation for a convection-diffusion process ϕ is the dependent variable, ρ is the density, $\mathbf{u}$ is the flow velocity, Γ is the diffusion coefficient, and S is the source term. ϕ can stand for mass fraction of a chemical species, enthalpy or temperature, a component of the velocity, or turbulent kinetic energy. For each meaning of ϕ, the appropriate meaning is given to S and Γ.

In two dimensions with no source term, the steady state equation reduces to

$$\frac{\partial J_x}{\partial x} + \frac{\partial J_y}{\partial y} = 0 \tag{3.2}$$

where the total (convection plus diffusion) fluxes are

$$\begin{aligned} J_x &\equiv \rho u\phi - \Gamma\frac{\partial\phi}{\partial x} \\ J_y &\equiv \rho v\phi - \Gamma\frac{\partial\phi}{\partial y} \end{aligned} \tag{3.3}$$

The pressure in the air bearing is found using a finite volume method to solve the Reynolds-type equation including thermal creep flow based on linearized Boltzmann theory [8]. In order to derive a generalized Reynolds-type lubrication equation, Fukui and Kaneko need to accurately estimate the mass flowrate per unit

channel width, $\dot{M}$, in the lubrication film [8]. The mass flow conservation law is used to derive their final result: a generalized lubrication equation including thermal creep flow.

In this model, the total flow rate $\dot{M}$ is the sum of the Poiseuille flow rate $\dot{M}_P$ due to the pressure gradient $\frac{dP}{dX}$, the Couette flow rate $\dot{M}_C$ due to the moving boundary, and thermal creep flow $\dot{M}_T$ due to a temperature gradient in the boundary $\frac{d\tau_w}{dX}$.

$$\dot{M} = \dot{M}_P + \dot{M}_C + \dot{M}_T$$

The flowrate of Couette flow is independent of the Knudsen number and is simply the solution to the continuum Couette flow problem for a plate moving at speed U and with a spacing h:

$$\dot{M}_C = \frac{\rho U h}{2}$$

The Poiseuille and thermal creep mass flowrates can calculated from expressions [12, Eqns. 86-87] semi-analytically obtained by Loyalka using the variational method to solve the linearized Boltzmann equation as shown in the previous chapter. These expressions were derived for the simplified case of a parallel plate channel and a collision process described by the BGK model with diffuse reflections at the walls.

Using the mass flowrates just discussed, Fukui and Kaneko expressed the non-dimensionalized two dimensional steady-state lubrication equation as follows:

$$\frac{\partial}{\partial X}\left\{\overline{Q}_P P H^3 \frac{\partial P}{\partial X} - \overline{Q}_T \frac{\partial \tau_w}{\partial X} P^2 H^3 - \Lambda_x P H\right\} + \frac{\partial}{\partial Y}\underbrace{\left\{\overline{Q}_P P H^3 \frac{\partial P}{\partial Y}\right.}_{\text{Poiseuille flow "diffusion"}} - \underbrace{\overline{Q}_T \frac{\partial \tau_w}{\partial Y} P^2 H^3}_{\text{thermal creep "convection"}} - \underbrace{\left.\Lambda_y P H\right\}}_{\text{Couette flow "convection"}} = 0 \quad (3.4)$$

Equation 3.4 is a special case of the general convection-diffusion differential equation 3.1. In former CML student Sha Lu's dissertation [14], the absence of thermal creep made direct substitution of the above values into Equation 3.3 straightforward: $\phi = P$, $\rho = H$, $\Gamma = \overline{Q}_P P H^3$, $u = \Lambda_x$ and $v = \Lambda_y$.

$$\begin{aligned} \Lambda_x &= u\frac{6\mu L}{p_a h_m^2} \\ \Lambda_y &= v\frac{6\mu L}{p_a h_m^2} \end{aligned} \quad (3.5)$$

are the bearing numbers in the X and Y directions, u and v are the X and Y velocity components. Note that u and v still have dimensions while $X = \frac{x}{L}$ and $Y = \frac{y}{L}$ are the non-dimensionalized slider length and width directions, respectively.

Here, consider thermal creep to be an additional convection term. Poiseuille flow, the gradient-driven diffusion term in Lu's application, is the result of a pressure gradient in the air bearing, while thermal creep is due to a temperature gradient in the boundary wall. Thus thermal creep is not a result of a gradient in the unknown field quantity P, and is therefore summed with Couette flow to form a total convection term. In addition, the thermal creep term maybe written as $\Omega_x PH$, of the same form as the Couette flow term $\Lambda_x PH$. Introduce

$$\begin{aligned} \Omega_x &= \overline{Q}_T \frac{\partial \tau_w}{\partial X} PH^2 \\ \Omega_y &= \overline{Q}_T \frac{\partial \tau_w}{\partial Y} PH^2 \end{aligned} \tag{3.6}$$

as the thermal creep coefficients in the X and Y directions. The substituted values for the flow velocity components becomes $u = \Lambda_x + \Omega_x$, $v = \Lambda_y + \Omega_y$. Thermal creep is an additional contribution to the convection (not pressure gradient driven) flow and Ω_x and Ω_y have been added to u and v

The total fluxes, the sum of convection, diffusion and thermal creep, become:

$$\begin{aligned} J_x &\equiv (\Lambda_x + \Omega_x) PH - \Gamma \frac{\partial P}{\partial X} \\ J_y &\equiv (\Lambda_y + \Omega_y) PH - \Gamma \frac{\partial P}{\partial Y} \end{aligned} \tag{3.7}$$

3.2 Discretization of Governing Differential Equation

Figure 3.1 is a schematic of a control volume surrounding node P with neighboring nodes E, W, N, and S. The associated interfaces of the control volume are denoted e, w, n, and s.

Integrate the steady-state governing differential equation, Equation 3.2, over the control volume. Consider the control volume to be of unit depth into the page. The resulting steady-state integrated discretized differential equation is:

$$J_e - J_w + J_n - J_s = 0 \tag{3.8}$$

$J_e = (J_x \Delta Y)_e$ is the integrated total flux at control volume face e. The same notation applies for the other faces of the control volume.

The values of the unknown non-dimensionalized pressure P at interfaces is approximated using the central difference scheme. Following Patankar's notation,

$$(P)_e \approx \frac{P_P + P_E}{2} \qquad \left(\frac{\partial P}{\partial X}\right)_e \approx \frac{P_E - P_P}{(\delta X)_e}$$

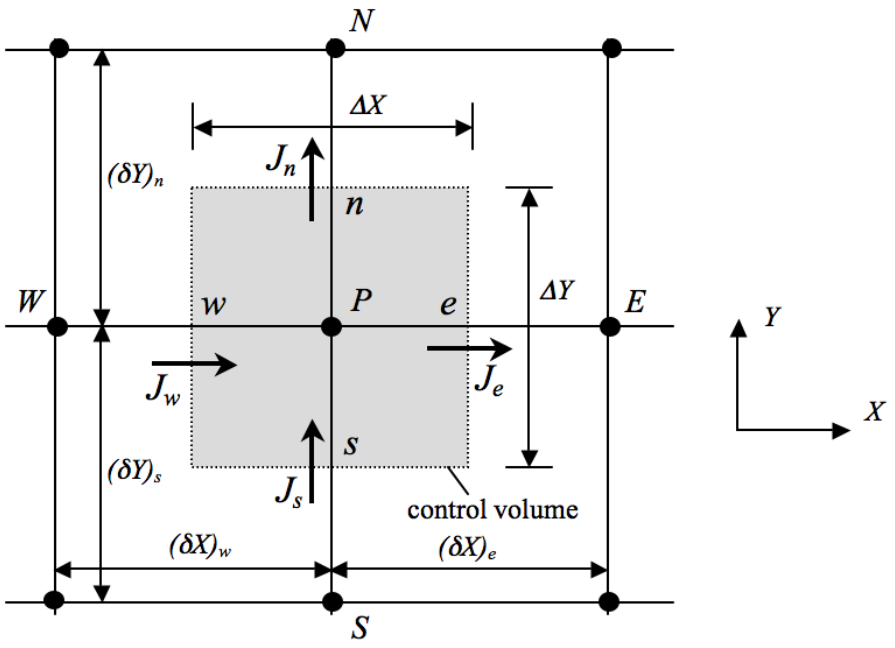

Figure 3.1: Control volume after Patankar [16]. Capital letters signify nodes while lower case letters signify interfaces of the control volume that lie between nodes.

$$
\begin{aligned}
(P)_w &\approx \frac{P_P + P_W}{2} & \left(\frac{\partial P}{\partial X}\right)_w &\approx \frac{P_P - P_W}{(\delta X)_w} \\
(P)_n &\approx \frac{P_P + P_N}{2} & \left(\frac{\partial P}{\partial Y}\right)_n &\approx \frac{P_N - P_P}{(\delta Y)_n} \\
(P)_s &\approx \frac{P_P + P_S}{2} & \left(\frac{\partial P}{\partial Y}\right)_s &\approx \frac{P_P - P_S}{(\delta Y)_s}
\end{aligned}
$$

Take J_e for example:

$$
\begin{aligned}
J_e &= \left\{((\Lambda_x + \Omega_x)PH)_e - \left(\Gamma \frac{\partial P}{\partial X}\right)_e\right\} \Delta Y \\
&= ((\Lambda_x + \Omega_x)H)_e \frac{P_P + P_E}{2} - \Gamma_e \left(\frac{P_E - P_P}{(\delta X)_e}\right) \Delta Y \\
&= \left[\frac{1}{2}(\Lambda_x H + \Omega_x H)_e \Delta Y + \frac{\Gamma_e \Delta Y}{(\delta X)_e}\right] P_P + \left[\frac{1}{2}(\Lambda_x H + \Omega_x H)_e \Delta Y - \frac{\Gamma_e \Delta Y}{(\delta X)_e}\right] P_E \\
&= \left[D_e + \frac{F_e + G_e}{2}\right] P_P - \left[D_e - \frac{F_e + G_E}{2}\right] P_E
\end{aligned}
$$

Define coefficients as follows.

Convection coefficients:

$$F_e = (\Lambda_x H)_e \Delta Y \tag{3.9a}$$
$$F_w = (\Lambda_x H)_w \Delta Y \tag{3.9b}$$
$$F_n = (\Lambda_y H)_n \Delta X \tag{3.9c}$$
$$F_s = (\Lambda_y H)_s \Delta X \tag{3.9d}$$

Thermal creep coefficients:

$$G_e = (\Omega_x H)_e \Delta Y \tag{3.10a}$$
$$G_w = (\Omega_x H)_w \Delta Y \tag{3.10b}$$
$$G_n = (\Omega_y H)_n \Delta X \tag{3.10c}$$
$$G_s = (\Omega_y H)_s \Delta X \tag{3.10d}$$

Diffusion coefficients:

$$D_e = \frac{\Gamma_e \Delta Y}{(\delta X)_e} \tag{3.11a}$$
$$D_w = \frac{\Gamma_w \Delta Y}{(\delta X)_w} \tag{3.11b}$$
$$D_n = \frac{\Gamma_n \Delta X}{(\delta Y)_n} \tag{3.11c}$$
$$D_s = \frac{\Gamma_s \Delta X}{(\delta Y)_s} \tag{3.11d}$$

The two dimensional steady-state momentum balance Equation 3.2 can be written in terms of the convection coefficients F, the thermal creep coefficients G, the diffusion coefficients D, the node of interest P, and the neighboring nodes E, W, N, and S. In an unfortunate convergence of nomenclature, the unknown field quantity to be solved for is the non-dimensionalized perssure P. The pressure value at the node P which is surrounded by the control volume is denoted P_P, and is similarly notated for the neighboring nodes.

$$a_P P_P = a_E P_E + a_W P_W + a_N P_N + a_S P_S + b \tag{3.12}$$

where

$$a_E = D_e - \frac{1}{2}(F_e + G_e) \tag{3.13a}$$
$$a_W = D_w + \frac{1}{2}(F_w + G_w) \tag{3.13b}$$

$$a_N = D_n - \frac{1}{2}(F_n + G_n) \tag{3.13c}$$

$$a_S = D_s + \frac{1}{2}(F_s + G_s) \tag{3.13d}$$

$$a_P = a_E + a_W + a_N + a_S \tag{3.13e}$$

$$b = 0 \tag{3.13f}$$

It is possible for coefficients in Equation 3.13 to become negative, which can result in unrealistic solutions or divergence of the solution. This problem will be remedied in the next section.

3.3 Stability of the Solution

Going back to the notation of the general differential equation, $F \equiv \rho u$ is the strength of convection and can be positive or negative, depending on the direction of the fluid flow. $D \equiv \frac{\Gamma}{\delta x}$ is the diffusion conductance and is always positive. For the air bearing application the convection is the sum of Couette flow and thermal creep contributions, and the strength of convection is $F + G = (\Lambda + \Omega)H\Delta Y$. The diffusion conductance in this application is $D = \frac{\Gamma \Delta Y}{(\delta X)}$.

The Peclet Number Pe$\equiv \frac{\rho u L}{\Gamma}$ is the ratio of the strengths of convection and diffusion. In the application under consideration, Pe can then be written as:

$$\text{Pe} \equiv \frac{F+G}{D} = \frac{(\Lambda+\Omega)H\Delta Y}{\Gamma \Delta Y/\delta X} = \frac{(\Lambda+\Omega)H}{\Gamma/\delta X} \tag{3.14}$$

The coefficients arise in Equation 3.13 are negative if $|\text{Pe}| > 2$, which lead to divergence of the solution.

The steady discretized continuity equation is

$$F_e + G_e - F_w - G_w + F_n + G_n - F_s - G_s = 0$$

Destability can arise if continuity is not identically satisfied, that is the net fluxes of the convective terms due to Couette and thermal creep flows do not sum to zero. An imperfect pressure field will be obtained at intermediate iterations until final convergence is attained. If the sum of the F's and G's is negative, then $a_P < \sum a_{nb}$ and the solution is destabilized. Remedy this problem by setting

$$a_P = a_E + a_W + a_N + a_S + \max(0, F_e + G_e - F_w - G_w + F_n + G_n - F_s - G_s) \tag{3.15a}$$

$$b = \max(0, F_w + G_w - F_e - G_e + F_s + G_s - F_n - G_n)P_P \tag{3.15b}$$

where P_P is the most current value of the unknown pressure at the control volume point P.

Many schemes have been developed to overcome the stability problems inherent in the central difference scheme used to discretize the differential equation (Patankar 1980 Chapter 5). Lu (1997) determined that out of the various stable convective schemes, the hybrid method is most suitable for the air bearing problem. In the hybrid method, a central difference scheme is used until $|\mathrm{Pe}| > 2$, then the upwind scheme is employed in which the diffusion terms has been set to zero (convection dominated).

$$
\begin{aligned}
a_E &= D_e A(|\mathrm{Pe}_e|) + \max(-(F_e + G_e), 0) && \text{(3.16a)}\\
a_W &= D_e A(|\mathrm{Pe}_w|) + \max(F_w + G_w, 0) && \text{(3.16b)}\\
a_N &= D_n A(|\mathrm{Pe}_n|) + \max(-(F_n + G_n), 0) && \text{(3.16c)}\\
a_S &= D_s A(|\mathrm{Pe}_s|) + \max(F_s + G_s, 0) && \text{(3.16d)}\\
a_P &= a_E + a_W + a_N + a_S + \\
&\quad \max(0, F_e + G_e - F_w - G_w + F_n + G_n - F_s - G_s) && \text{(3.16e)}\\
b &= \max(0, F_w + G_w - F_e - G_e + F_s + G_s - F_n - G_n) P_P && \text{(3.16f)}
\end{aligned}
$$

where the function $A(|\mathrm{Pe}|)$ for the hybrid scheme is

$$A(|\mathrm{Pe}|) = \max(0, 1 - 0.5|\mathrm{Pe}|) \tag{3.17}$$

Chapter 4

Semi-analytical Solutions to Infinitely Long Parallel Plate-Slider Bearing

Consider an infinitely long parallel-surface slider air bearings pictured in Figure 4.1. Thermal creep flow between parallel plates has been analyzed by many authors [12, 13, 4], so simulation of this same problem can be verified with published results. Figure 4.1 is the scenario that will be investigated semi-analytically and analytically, and then these results are compared with the simulation results from the new CMLAir QuickHAMR that includes thermal creep.

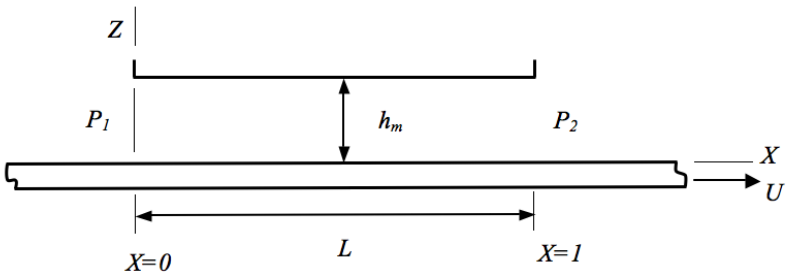

Figure 4.1: Infinitely long parallel-surface slider air bearing. This simple problem is used to validate the implementation of thermal creep into CMLAir.

4.1 Continuum Lubrication Theory

In *Fluid Film Lubrication* [10, Ch. 3], analytical solutions to lubrication analysis for simple, infinitely long slider, roller and journal bearings are presented. Infinite-length fluid films are easier to analyze and relatively simple closed-form solutions can be obtained for the pressure distribution, load capacity, friction force on the moving surface, center of pressure, and mass flow. The limiting solution for infinitely long parallel-surface slider bearings for a gas film for $\Lambda = 0$ will be used to reason why the pressure will remain ambient within the bearing.

For gas films only, when the infinite boundary surface is stationary $U = 0$ ($\Lambda \to 0$), the solution for the non-dimensionalized pressure P is:

$$P = \left[1 + (P_2^2 - 1)X\right]^{1/2} \tag{4.1}$$

In CMLAir Quick 4.32, the boundary condition for pressure is ambient ($P = 1$) at the edges of the slider. For these boundary conditions $P_2 = 1$ and therefore $P = 1$ everywhere in the bearing from $X = 0$ to $X = 1$. The mass flow into the bearing for this case is

$$m' = -\frac{P_2^2 - 1}{24} = 0$$

It makes sense for this boring case that the air is just 'sitting there' between the two plates. No pressure difference and no relative velocity means air is not flowing in the continuum case.

Extrapolate this pressure distribution to the case where the plates are held fixed so they don't collapse since the air bearing won't support a gap. Now introduce a linear temperature gradient on the boundary surfaces. Since the spacing is constant and the temperature gradient is constant in the whole air bearing domain, it is reasonable considering the continuum solution just discussed to assume that the pressure is ambient in the air bearing and $\frac{dP}{dX} = 0$ everywhere. In other words, the only mass flow will be due to thermal creep since the pressure gradient is zero (no Poiseuille flow) and the relative motion between the boundary surfaces is zero (no Couette flow).

4.2 Semi-analytical Solution to FK Equation

Now use the conclusion of ambient pressure in the entire domain to solve the generalized lubrication equation based on the Boltzmann equation (abbreviated in following discussions as the FK equation). Since $\frac{dP}{dX} = 0$ and $\Lambda = 0$, the FK equation reduces to

$$\frac{d}{dX}\left[\overline{Q}_T(D)\frac{d\tau_w}{dX}P^2H^3\right] = 0$$

Here $P = 1$, $H = 1$, $\frac{d\tau_w}{dX}$ is constant, and $\overline{Q}_T(D)$ is constant for a given value of D, so we can simply integrate:

$$\overline{Q}_T(D)\frac{d\tau_w}{dX}P^2H^3 = \text{constant}$$

In otherwords the mass flowrate is only due to thermal creep and is uniform in the domain. There are no reservoirs to store air at either end of the plate domain so no pressure head can develop as fluid creeps along the boundary walls from cold to hot (thermal creep). Therefore the pressure in ambient throughout the air bearing as assumed. Mass flowrate in X direction per unit slider width [kg/s/m]:

$$\dot{M} = \dot{M}_T = \overline{Q}_T\frac{d\tau_w}{dX}P^2H^3 \cdot \frac{D_0}{6}\frac{h_m^2 p_0}{L\sqrt{2RT_0}} \tag{4.2}$$

Rewrite Equation 4.2 to highlight the trend of $\dot{M}_T$ with Knudsen number:

$$\dot{M}_T = PH^2\frac{d\tau_w}{dX}\frac{p_0\lambda^2}{L\sqrt{2RT_0}} \cdot \frac{Q_T}{\text{Kn}^2} \tag{4.3}$$

The only quantities in the above equation that change with Kn if the reference condition remains standard atmospheric are Q_T and Kn^{-2}. The plot of Q_T vs Kn is approximately logarithmic and a logarithmic best fit curve of the form $a\log(\text{Kn})+b$ is found. The ratio of this Q_T fit curve to Kn^2 is plotted in Figure 4.2. The logarithmic increase of Q_T is dominated by Kn^{-2} so the overall trend is for $\dot{M}_T$ to decrease with increasing Knudsen number. Put differently, for ambient reference state, decreasing the spacing decreases the mass flow rate due to thermal creep between to parallel plates. $\dot{M}_T$ for different values of Kn are compared with simulation results in upcoming chapter in Table 5.2.

4.3 Semi-analytical Solution to Lubrication Equation with Velocity Slip Boundary Conditions

Microflows and Nanoflows [11] describes another method to evaluate the mass flow due to thermal creep between two parallel plates in the slip flow regime ($0.01 < \text{Kn} < .1$). In this regime the flow is governed by the compressible Navier Stokes equations and rarefaction effects are modeled with velocity slip and temperature jump boundary conditions.

For low Re flows and large aspect ratio channels $\frac{L}{h} \ll 1$ the inertial terms can be neglected. The momentum equation in streamwise direction (the same equation appears in the theory of [10]):

$$\frac{\partial p}{\partial x} = \mu\frac{\partial^2 u}{\partial z^2}$$

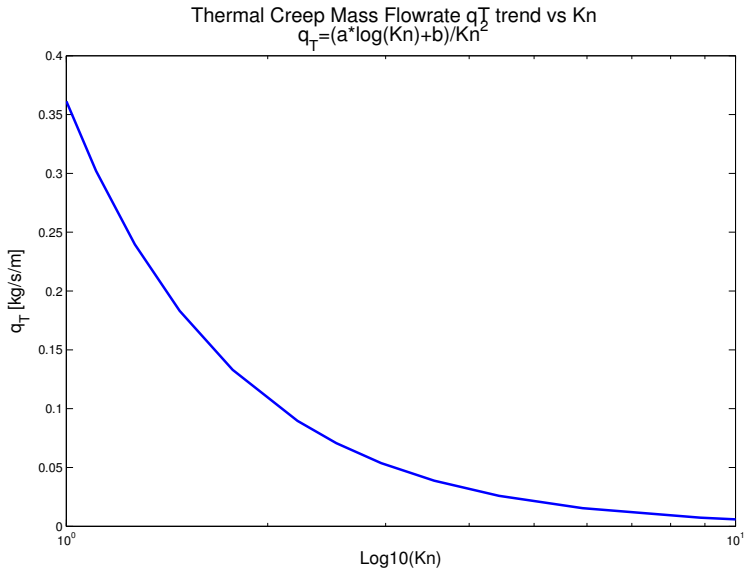

Figure 4.2: $\dot{M}_T$ trend with Kn.

The slip velocity boundary condition including thermal creep is:

$$u_s = \frac{1}{2}\left[\left(2-\sigma_v\right)u_\lambda + \sigma u_w\right] + u_c$$

where $u_c = \frac{3}{4}\frac{\mu R}{P}\frac{\partial T}{\partial s}$ is the thermal creep flow for rarefied flows with $\lambda < h$ is derived from the Boltzmann equation. It enchances the flow velocity near the wall. Integrating the momentum equation and enforcing slip velocity boundary conditions gives the velocity flow profile $u(z)$. The mass flow rate per unit channel depth [kg/s/m] follows from integrating the velocity profile and multiplying by the density $\dot{M} = \rho \int_0^h u(z)dz$:

$$\dot{M} = -\frac{h^3 P}{12\mu RT}\frac{dP}{dX}\left[1 + 6\frac{2-\sigma_v}{\sigma_v}(\mathrm{Kn} - \mathrm{Kn}^2)\right] + \frac{3}{4}\frac{\mu h}{T}\frac{dT}{dx} \tag{4.4}$$

It has already been argued for this problem $\frac{dP}{dX} = 0$. So the steady-state velocity due to thermal creep can be approximated by

$$\dot{M}_{T,ss} = \frac{3}{4}\frac{\overline{\mu} h}{\overline{T}}\frac{dT}{dX}$$

where $\overline{\mu}$ is evaluated at the average temperature. Results for different Knudsen numbers appear in the next chapter in Table 5.2.

Chapter 5

Simulation of Infinitely Long Parallel Plate-Slider Bearing

Simulation of the parallel-plate slider was done with the new CMLAir Quick-HAMR, the static air bearing solver with thermal creep added. The simulation parameters for a small temperature gradient ($\frac{\partial \tau_w}{\partial X} = \frac{1}{3} \ll 1$) are in Table 5.1. The notation for temperature follows that for pressure: T_1 is the temperature at $X = 0$ and T_2 is the temperature at $X = 1$. Note that is was an extreme case for the static solver to run: 0 rpm, no rails or recess, fixed attitude solution. But the air bearing solver still ran and outputted what was expected: ambient pressure in the whole domain, no Poiseuille or Couette flow, and uniform thermal creep flow in the direction of the temperature gradient. Table 5.2 contains the simulation results for the parameters in Table 5.1. The simulation results match semi-analytical mass flow rate $\dot{M}_{T,FK}$ from Section 4.2 within three significant digits and closely match the slip flow result $\dot{M}_{T,ss}$ of Section 4.3. All show the same trend: thermal creep mass flow rate decreases with decreased spacing.

Table 5.1: Small temperature gradient simulation parameters.

p_0	1 atm
$T_0 = T_1$	25°C
T_2	125°C
$\frac{\partial \tau_w}{\partial X}$	$\frac{1}{3}$
L	0.85 mm
Grid size	49x49 uniform

A temperature jump of only 100°C over the entire length of the slider would be very small in a HAMR HDD. For a 4 Tb/in^2 HDD, a bit radius of 6.35 nm is needed. HAMR magnetic media will need to be heated 300-400 K above ambient

temperature, so estimate $\Delta T = 350$ K. For $T_0 = 300$ K and $L = 0.85$ mm, the non-dimensionalized temperature gradient is

$$\frac{d\tau}{dX} = 156168 \sim \mathcal{O}(10^5)$$

This is a very large temperature gradient and outside the assumptions for the linearized Boltzmann equation. But proceed with a simulation with this large gradient to obtain an estimate of a HAMR mass flow rate and velocity.

All the parameters for this fixed attitude solution for a flat, rail-less slider design simulation are give in Table 5.3. FK equation semi-analytical and simulation results for this temperature gradient are given in Table 5.4.

Comparison of the magnitudes of the mass flow rates in Tables 5.2 and 5.4 show that mass flow rate is proportional to the boundary temperature gradient. Increasing the temperature gradient by a factor of ~ 468500 resulted in the same factor increase in thermal creep mass flow rate for the range of Knudsen numbers studied. This trend has been proved using the linear Boltzmann equation in [4].

Whereas the small temperature gradient has film thickness-averaged velocities on the order of nm/s, the velocities for the HAMR temperature gradient were on the order of cm/s. For comparison, the speed of the airflow in a conventional HDD can be expected to be on the order of the linear speed of the disk, $\mathcal{O}(10)$ m/s. So the contribution of thermal creep to the mass flow will be small. So in full slider simulations with a laser spot at the trailing edge center, thermal creep can be expected to only locally modifying the flow and probably not enough to warrant air bearing surface design modifications.

Table 5.2: $\dot{M}_T$ vs. Kn study with semi-analytical FK equation, slip theory, and simulation results. Corresponding spacing h_m is also indicated. u_{ave} is the thickness averaged velocity based on the simulation results.

Kn	h_m (nm)	$\dot{M}_{T,FK}$	$\dot{M}_{T,ss}$	$\dot{M}_{T,simul}$	u_{ave} (nm/s)
1	68.6	1.4108e-10	3.5900e-10	1.4097e-10	25.3
5	13.72	1.0503e-11	7.1798e-11	1.0500e-11	9.43
10	6.86	3.2565e-12	3.5899e-11	3.2556e-12	5.85

Table 5.3: Small temperature gradient simulation parameters.

p_0	1 atm
$T_0 = T_1$	25°C
T_2	375°C
$\frac{\partial \tau_w}{\partial X}$	156168
L	0.85 mm
Grid size	49x49 uniform

Table 5.4: $\dot{M}_T$ vs. Kn study for a HAMR temperature gradient results for the FK equation semi-analytical and simulation. Corresponding spacing h_m is also indicated. u_{ave} is the thickness averaged velocity based on the simulation results.

Kn	h_m (nm)	$\dot{M}_{T,FK}$	$\dot{M}_{T,simul}$	u_{ave} (cm/s)
1	68.6	6.610e-5	6.604e-5	12
5	13.72	4.921e-6	4.919e-6	4.4
10	6.86	1.526e-6	1.525e-6	2.7

Chapter 6

Preliminary Trailing Pad Simulation

Since $\dot{M}_T = 0$ when $\frac{\partial \tau_w}{\partial X}$, thermal creep will only occur over the laser spot at the center of the trailing pad and will be very localized to an area with a diameter of $\mathcal{O}(100)$ nm. In order to get a fine grid that would capture the laser spot in more than just the one node possible with the full slider simulation, just a portion of the trailing pad was simulated. CMLAir Quick 4.32 was used to determine the trailing edge center (TEC) fly height, pitch, and roll (flying attitude) of the slider design. To simulate the slider, a 0.025 mm square (the width of the trailing pad) flat plate at this fixed attitude solution with a spinning disk was executed. The boundary temperature used, which corresponds to the HAMR disk surface, is depicted in Figure 6.1. The spacing if the trailing pad portion as determined by the slider static attitude is plotted in Figure 6.2.

The thermal creep mass flow rate vector field plotted in Figure 6.3 shows that thermal creep flow is contained over the laser spot and follows the temperature gradient, as expected. The largest value of $\dot{M}_T$ realized at the TEC is $\mathcal{O}(10^{-7})$ kg/s/m. Simulations of the full slider without a temperature gradient show an $\dot{M} = \dot{M}_P + \dot{M}_C$ of the size $\mathcal{O}(10^{-3})$ kg/s/m. So in a very localized area, thermal creep due to the disk laser spot will slightly enhance the total mass flow rate.

Recall that the purpose of CMLAir is to solve for the unknown P in the FK equation and determine the pressure distribution under the slider. Other quantities can be derived from the pressure: pressure force, air shearing force on the lubricant, center of total pressure force, mass flow streamlines. This author has added mass flow rates and a thickness-averaged velocity to outputted derived quantities. So to evaluate the effect of thermal creep, the effect on pressure must be investigated.

Compared with the case of an isothermal, ambient temperature disk, the pressure distribution was not significantly affected. The pressure in the control volumes directly above the $\sim$ 200 nm radius laser spot decrease 10-20%. Within a $\sim$ 500

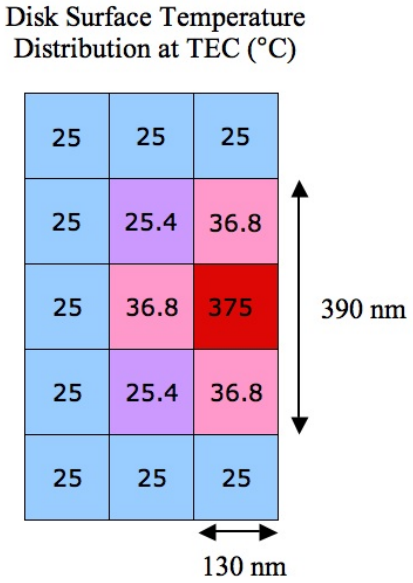

Figure 6.1: Trailing pad simulation boundary temperature distribution corresponding to laser heating of the disk at the TEC.

nm radius of the laser spot center the pressure decreased $\mathcal{O}(1\%)$. So an area about $2.5^2 = 6.25$ times the area of the laser spot saw a slight decrease in pressure. Decrease in pressure with increasing mass flow rate (or velocity) in subsonic flow can be qualitatively explained with incompressible flow behavior. For steady, frictionless flow and neglecting potential energy changes, Bernoulli's equation says that along a streamline

$$\frac{p}{\rho} + \frac{u^2}{2} = \text{constant}$$

So for constant density, an increase in velocity is accompanied by a decrease in pressure. However, the pressure force and the center of the pressure force were unaffected. The decrease in pressure was too small and over too small of an area to change the force when integrating over the trailing pad. Thus thermal creep due to the laser spot on the disk can be considered negligible.

More boundary temperature gradients will be realized once a heat transfer model between the slider and disk is developed and the surface temperatures of the disk and slider found with numerical simulation. For this report, the thermal creep results are just for an estimated disk surface temperature distribution.

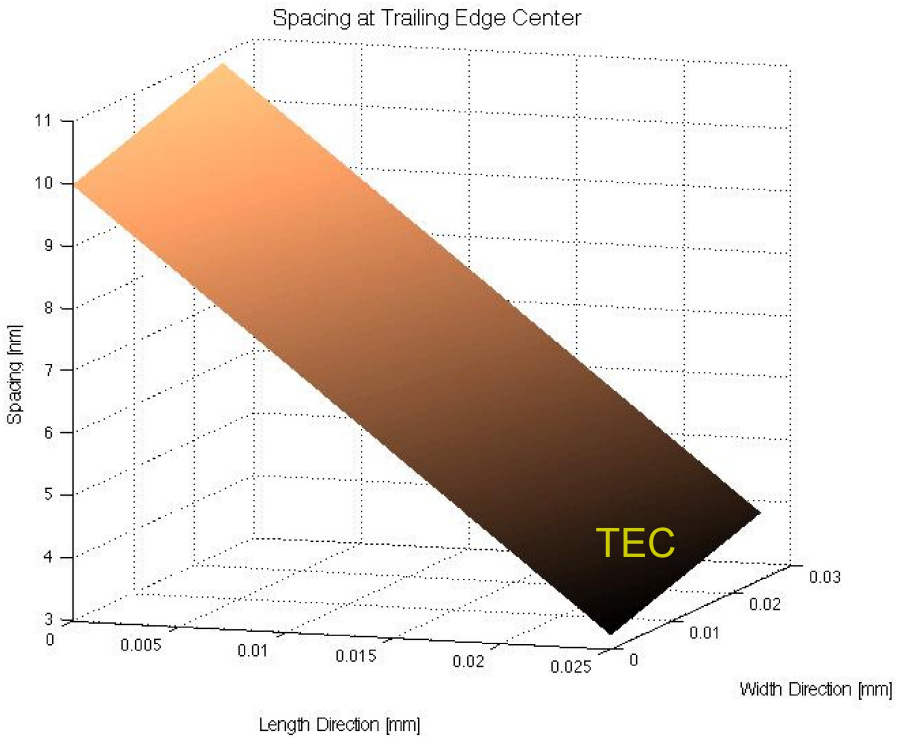

Figure 6.2: Trailing pad simulation fixed attitude.

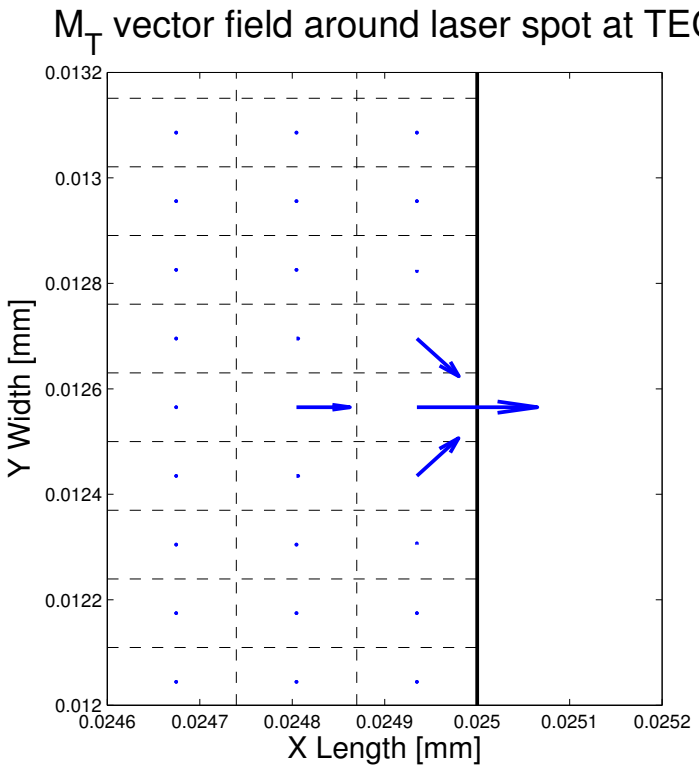

Figure 6.3: $\dot{M}_T$ vector field for the trailing pad simulation. The vector at the TEC has been scaled smaller because it is two orders of magnitude greater than the rest.

Chapter 7

Future Work

The implementation of thermal creep into the air bearing solver was the first step in creating a HAMR HDD model. Next the heat transfer between the disk and slider will be implemented by creating an iterative solver between CMLAir Quick HAMR and a finite element solver, as was done for the TFC CMLAir code developed by Jinglin Zheng. Thermal distortion of the disk and slider will be computed using a commercial finite element solver. The model will iterate between the finite volume solution to the air bearing and the finite element solution for the disk and slider. Conduction through the air bearing is the other mode of heat transfer and a flux expression for it is derived from first-order slip theory that has been shown to agree well with experimental results [5]. Near-field effects have the potential to drastically enhance irradiation if the layered materials making up the slider and disk complement each other. The slider and disk can be considered two half spaces (Al_2O_3/TiC and Co, respectively) each with a 1 nm DLC overcoat layer separated by a 2 nm vacuum gap. The dielectric function of these materials have to be determined. The thermal radiation in this one-dimensional layered media will be evaluated using dyadic Green's functions and the scattering matrix method [7].

Looking further ahead, a lubricant flow model based on lubrication theory will predict the transient lubrication depletion [17]. After a static model is complete, transience will be added to make a realistic dynamic HAMR model.

Note: Contact the author for color figures: jobechtel@gmail.com

Bibliography

[1] M. Abramowitz and I.A. Stegun. *Handbook of Mathematical Functions*. Dover, 1968.

[2] E.J. Black, J.A. Bain, and T.E. Schlesinger. Thermal management in heat-assisted magnetic recording. *IEEE Transactions on Magnetics*, 43(1):62–66, January 2007.

[3] W.A. Challener, C. Peng, A.V. Itagi, D. Karns, W. Peng, Y. Peng, X. Yang, X. Zhu, N.J. Gokemeijer, Y.-T. Hsia, G. Ju, R.E. Rottmayer, and M.A. Seigler. Heat-assisted magnetic recording by a near-field transducer with efficient optical energy transfer. *Nature Photonics*, 3:220–224, 2009.

[4] C.-C. Chen, I. Chen, T.-P. Liu, and Y. Sone. Thermal transpiration for the linearized boltzmann equation. *Communications on Pure and Applied Mathematics*, 60(2):147–163, 2007.

[5] D. Chen, N. Liu, and D.B. Bogy. A phenomenological heat transfer model for the molecular gas lubrication system in hard disk drives. *Journal of Applied Physics*, 105:084303, 2009.

[6] Information Storage Industry Consortium. EHDR Program. `http://www.insic.org/programs_EHDR.html`, December 2009.

[7] M Francoeur, MP Menguc, and R Vaillon. Solution of near-field thermal radiation in one-dimensional layered media using dyadic green's functions and the scattering matrix method. *Journal Of Quantitative Spectroscopy & Radiative Transfer*, 110(18):2002–2018, 2009.

[8] S. Fukui and R. Kaneko. Analysis of ultra-thin gas film lubrication based on linearized boltzmann equation: First report derivation of a generalized lubrication equation including thermal creep flow. *ASME Journal of Tribology*, 110:253–262, 1988.

[9] S. Fukui and R. Kaneko. A database for interpolation of poiseuille flow rates for high knudsen number lubrication problems. *Journal of Tribology*, 112:78–83, 1990.

[10] W.A. Gross, L.A. Matsch, V. Castelli, A. Eshel, J.H. Vohr, and M. Wildmann. *Fluid Film Lubrication*. John Wiley & Sons, Inc., New York, 1980.

[11] G. Karniadakis, A. Beskok, and N. Aluru. *Microflows and Nanoflows: Fundamentals and Simulation*. Springer Science+Business Media, Inc., New York, 2005.

[12] SK Loyalka. Kinetic theory of thermal transpiration and mechanocaloric effect. i. *The Journal of Chemical Physics*, 55(9):4497–4503, 1971.

[13] SK Loyalka. Comments on "poiseuille flow and thermal creep of a rarefied gas between parallel plates". *Physics of Fluids*, 17(5):1053–1055, 1974.

[14] S. Lu. *Numerical Simulation of Slider Air Bearings*. PhD thesis, University of California at Berkeley, 1997.

[15] AJ Macleod. Chebyshev expansions for abramowitz functions. *Applied Numerical Mathematics*, 10(2):129–137, 1992.

[16] S.V. Patankar. *Numerical Heat Transfer and Fluid Flow*. Hemisphere Publishing Corporation, 1980.

[17] L. Wu. Modelling and simulation of the lubricant depletion process induced by laser heating in heat-assisted magnetic recording system. *Nanotechnology*, 18:215702, 2007.

[18] B.X. Xu, H.X. Yuan, J. Zhang, J.P. Yang, R. Ji, and T.C. Chong. Thermal effect on slider flight height in heat assisted magnetic recording. *Journal of Applied Physics*, 103(7):07F525, 2008.